Personalized Medicine and Imaging

Clinical Cancer Research

Correlation between Ferumoxytol Uptake in Tumor Lesions by MRI and Response to Nanoliposomal Irinotecan in Patients with Advanced Solid Tumors: A Pilot Study

Ramesh K. Ramanathan[1,2], Ronald L. Korn[1,3], Natarajan Raghunand[4], Jasgit C. Sachdev[1], Ronald G. Newbold[1,3], Gayle Jameson[1], Gerald J. Fetterly[5], Joshua Prey[5], Stephan G. Klinz[6], Jaeyeon Kim[6], Jason Cain[6], Bart S. Hendriks[6], Daryl C. Drummond[6], Eliel Bayever[6], and Jonathan B. Fitzgerald[6]

Abstract

Purpose: To determine whether deposition characteristics of ferumoxytol (FMX) iron nanoparticles in tumors, identified by quantitative MRI, may predict tumor lesion response to nanoliposomal irinotecan (nal-IRI).

Experimental Design: Eligible patients with previously treated solid tumors had FMX-MRI scans before and following (1, 24, and 72 hours) FMX injection. After MRI acquisition, R2* signal was used to calculate FMX levels in plasma, reference tissue, and tumor lesions by comparison with a phantom-based standard curve. Patients then received nal-IRI (70 mg/m^2 free base strength) biweekly until progression. Two percutaneous core biopsies were collected from selected tumor lesions 72 hours after FMX or nal-IRI.

Results: Iron particle levels were quantified by FMX-MRI in plasma, reference tissues, and tumor lesions in 13 of 15 eligible patients. On the basis of a mechanistic pharmacokinetic model, tissue permeability to FMX correlated with early FMX-MRI signals at 1 and 24 hours, while FMX tissue binding contributed at 72 hours. Higher FMX levels (ranked relative to median value of multiple evaluable lesions from 9 patients) were significantly associated with reduction in lesion size by RECIST v1.1 at early time points ($P < 0.001$ at 1 hour and $P < 0.003$ at 24 hours FMX-MRI, one-way ANOVA). No association was observed with post-FMX levels at 72 hours. Irinotecan drug levels in lesions correlated with patient's time on treatment (Spearman $\rho = 0.7824$; $P = 0.0016$).

Conclusions: Correlation between FMX levels in tumor lesions and nal-IRI activity suggests that lesion permeability to FMX and subsequent tumor uptake may be a useful noninvasive and predictive biomarker for nal-IRI response in patients with solid tumors. *Clin Cancer Res; 23(14); 3638–48. ©2017 AACR.*

Introduction

Liposomal drug delivery carriers can enhance utility of existing anticancer drugs by shielding the encapsulated drug from rapid clearance and metabolism, and extending mean residence time in plasma and tumor tissue (1, 2). Aberrant characteristics in the tumor neovasculature and microenvironment lead to passive accumulation of nanomedicines and macromolecular drugs in tumor lesions, which is known as the enhanced permeability and retention (EPR) effect (3, 4). The extent to which the EPR effect occurs in humans is controversial and subject to debate. Existing data suggest the EPR effect is highly variable across tumor lesions (5) and may be heavily influenced by the tumor microenvironment (6). Rationales for noninvasive imaging aimed toward selection of patients with a sufficiently high level of lesion-specific nanotherapeutic accumulation have been proposed (7, 8); however, clinical implementation has been limited (4, 9).

Nanoliposomal irinotecan (nal-IRI; Onivyde, irinotecan liposome injection, MM-398, PEP02, BAX2398) comprises irinotecan encapsulated in a nanoparticle drug delivery system in the form of the irinotecan sucrose octasulfate salt with an average particle size of 110 nm (10, 11). Nal-IRI in combination with 5-fluorouracil/leucovorin (5-FU/LV) is approved for use in the United States, European Union, and Taiwan Health Authorities for the treatment of patients with metastatic pancreatic cancer after disease progression following gemcitabine-based therapy (11, 12). The liposomal payload, irinotecan, is a member of the camptothecin class of topoisomerase I (TOP1) inhibitors and causes cell death through DNA damage after replication-fork collisions with transiently trapped drug–TOP1–DNA cleavage complexes, thus highlighting length of drug exposure as an important driver for

[1]Virginia G Piper Cancer Center, Honor Healthcare, Scottsdale, Arizona. [2]Translational Genomics Research Institute, Phoenix, Arizona. [3]Imaging Endpoints, Scottsdale, Arizona. [4]Moffitt Cancer Center, Tampa, Florida. [5]Roswell Park Cancer Institute, Buffalo, New York. [6]Merrimack Pharmaceuticals, Inc., Cambridge, Massachusetts.

Note: Supplementary data for this article are available at Clinical Cancer Research Online (http://clincancerres.aacrjournals.org/).

R.K. Ramanathan and R.L. Korn contributed equally to this article.

Current address for G.J. Fetterly: Athenex, Buffalo, New York; current address for E. Bayever: Glenmark Pharmaceuticals Inc., Mahwah, New Jersey; and current address for R. Ramanathan: Mayo Clinic Hospital, Phoenix, Arizona.

Corresponding Authors: Ramesh K. Ramanathan, Mayo Clinic Hospital, 5777 East Mayo Boulevard, Phoenix, AZ 85054. Phone: 480-302-6185; Fax: 480-323-1359; E-mail: Ramanathan.ramesh@mayo.edu; and Stephan G. Klinz, Merrimack Pharmaceuticals, One Kendall Square, Suite B7201, Cambridge, MA 02139. Phone: 617-441-7484; Fax: 617-491-1386; E-mail: Sklinz@merrimack.com

doi: 10.1158/1078-0432.CCR-16-1990

AACR

Translational Relevance

Liposomal or nanoparticle-based drug delivery partly depends on enhanced tumor permeability and retention (EPR) properties. Nanoparticle permeability rates are highly variable and differ from small drug molecules that readily diffuse across tumor vasculature. Therefore, standard DCE-MRI pharmacokinetic analysis using low-molecular weight contrast may not be suitable for evaluating tumor lesion permeability to nanoparticles. The ferumoxytol (FMX) iron oxide nanoparticle has pharmacokinetic properties similar to nal-IRI and may be appropriate for estimating EPR effects given its close particle size and longer retention in the blood compared with standard gadolinium-based contrast agents. Using a quantitative MRI approach, we estimated FMX levels in tumor lesions and demonstrated marked heterogeneity of tumor EPR effect. Higher FMX levels were associated with greater reduction in lesion size after nal-IRI treatment. This study suggests that quantitative FMX-MRI may serve as a predictive biomarker for nanoparticle-based drug delivery and may enable patient stratification according to comparatively high tumor uptake of such therapies.

cytotoxicity (13). Compared with pharmacokinetic data of non-liposomal irinotecan (14), nal-IRI is characterized by a higher exposure, lower clearance, and smaller volume of distribution.

Preclinical experiments (15) have demonstrated that nal-IRI greatly increased availability of the active metabolite of irinotecan, SN-38, in the tumor and showed dose-dependent antitumor efficacy at much lower doses than nonliposomal irinotecan. A semimechanistic pharmacokinetic model identified the duration of prolonged SN-38 levels above an intratumoral threshold as a major pharmacologic determinant for *in vivo* activity of irinotecan in mice. A sensitivity analysis found that pharmacokinetic properties and permeability of the tumor vasculature to nal-IRI positively affected duration of SN-38 in tumors. Liposomal deposition in tumors was also found to be a rate-limiting step for drug delivery to cells for other long-circulating liposomes (16). It has previously been shown that tumor deposition of a liposomal contrast agent correlated with treatment outcome to a liposomal drug in a rat xenograft model (17).

CT or MRI modalities have been used in clinical settings to assess tissue perfusion and permeability, particularly with small-molecule and macromolecular contrast media (18, 19). These studies demonstrated that permeability rates depended on molecular or particle properties such as hydrodynamic diameter and shape (4). Liposomal imaging agents based on single-photon emission computed tomographic (SPECT) or positron emission tomographic (PET) imaging have been examined as well (20–22). A widely studied class of imaging agents is superparamagnetic iron oxide nanoparticles, which have excellent MRI contrast characteristics and demonstrate concentration-related negative contrast on T2- and T2*-weighted sequences. Variable coatings applied to these particles can modulate their pharmacokinetic behavior. Longer-circulating iron oxide nanoparticles exhibit delayed enhancement and uptake into reactive cells within lesions (23, 24) and mirror pharmacokinetic and distribution characteristics seen for liposomes (25, 26) and similarly sized nanotherapeutics (27).

Ferumoxytol (FMX) is an approximately 750-kDa superparamagnetic iron oxide nanoparticle with an average colloidal particle size of 23 nm and a narrow particle size distribution ranging from 10 to 70 nm (28). FMX is approved to treat iron deficiency anemia in patients with chronic renal failure (29). FMX is composed of a nonstoichiometric magnetite core covered by a semi-synthetic carbohydrate coating of polyglucose sorbitol carboxymethyl ether. FMX has slower clearance and delayed enhancement properties compared with gadolinium-based contrast agents and also allows after tissue deposition visualization of inflammatory cells in vessel walls and tissue because of uptake of the nanoparticles by macrophages (24, 30). In preclinical studies, FMX did not interfere with the pharmacokinetics, biodistribution, or cellular distribution of liposomes within tumors (25). Broad colocalization of liposomes and FMX was observed in perivascular stromal areas, and correlation between the FMX-MRI signal and tumor drug uptake was seen particularly in tumors with high liposomal drug delivery (25). Comparable results were reported with PLGA-PEG–based polymeric therapeutic nanoparticles (27). We hypothesized that FMX-MRI could be used as a clinical imaging approach for predicting delivery to tumor lesions and subsequent antitumor activity of nanotherapeutics. Here we measure the deposition characteristics of FMX in tumor lesions using a quantitative MRI approach and compare them with tumor lesion responses after treatment with nal-IRI.

Materials and Methods

Study design

This publication describes the pilot phase of an ongoing institutional review board–approved clinical study (31) that was conducted at the Virginia G Piper Cancer Center in Scottsdale, AZ. The primary objective was to assess the feasibility of quantitative MRI to determine FMX levels in tumor lesions and to assess lesion biopsies for macrophage content and metabolite levels. A secondary endpoint was tumor response assessed by RECIST v1.1 every 8 weeks. Plasma samples to assess the PK of FMX and nal-IRI were collected. Data cut-off date for the pilot phase was February 20, 2015. For study procedures, see Supplementary Information and Supplementary Fig. S1.

Study criteria

Eligible patients were 18 years of age or older and had advanced solid tumors that had progressed while on $\geq$1 prior regimen, Eastern Cooperative Oncology Group performance status of 0, 1, or 2, and acceptable kidney, bone marrow, and liver function. All patients had metastatic disease with 2 lesions $\geq$2 cm in diameter, accessible for a percutaneous biopsy. Exclusion criteria included prior irinotecan or bevacizumab therapy within the preceding 6 months. Additional inclusion and exclusion criteria are available (31).

FMX and MRI phantom

Patients received FMX (AMAG Pharmaceuticals) intravenously at a dose of 5 mg/kg, delivered as a bolus injection (29) at 1 mg/second and capped at 510 mg. All FMX concentrations are expressed as amounts of elemental iron. After injection, patients were kept under observation for 30 minutes with continuous vital sign monitoring for possible signs of hypersensitivity reactions. Administration by bolus injection was consistent with FDA-approved labeling at the time of the study (29). Since the

completion of this pilot study, the original package insert for Feraheme (ferumoxytol injection) was changed in March 2015 from a bolus injection to an intravenous infusion over at least 15 minutes. Patients are to be observed for signs or symptoms of hypersensitivity reactions during and for at least 30 minutes following FMX infusion, including monitoring of blood pressure and pulse during and after FMX administration. These changes will be reflected in the design of all our ongoing and future clinical studies with FMX (29).

A FMX phantom was assembled consisting of 15-mL tubes with FMX at concentrations of 0, 10, 20, 30, 40, 50, 100, 150, or 200 μg/mL elemental iron in 2% agarose containing 5 mmol/L sodium azide. Agarose gel provides tissue equivalent phantom material for measuring contrast agent relaxivity (32). This phantom was included in all MRI scans of either patients or isolated plasma samples.

FMX-MRI acquisition

MRI for FMX relaxometry was acquired on a GE 1.5-T instrument with a series of 6 coregistered fat-suppressed fast spoiled gradient echo (FSPGR) scans with echo times (TE) of 1.5, 3.0, 4.5, 6.0, 9.0, and 13.2 milliseconds using a phased-array torso body coil (Supplementary Table S1). The FSPGR sequences started on average at 69 min after FMX injection [95% confidence interval (CI) 54–85 minutes], and TE acquisition averaged approximately 18 minutes. Slice thickness and spacing were 6 mm × 1 mm, using a 256 × 256 matrix with a field of view to match the size of the body part being imaged. T2* and R2* maps were fitted by linear regression of the log-transformed signal intensities at each echo. Mean T2* and R2* values were determined from operator-defined 2D regions of interest (ROI) circumscribing tumor lesions and select organ sites (liver, spleen, muscle) that were traced around the tissue–tumor interface of selected FMX-MRI target lesions on each FSGPR echo sequence. A FMX phantom was placed under the patient and included in the scan field of view.

For determination of FMX concentrations in plasma, samples of patient plasma were placed next to the FMX phantom and scanned using the same MRI acquisition series as for study patients.

FMX-MRI analysis

From each scan, the T2* relaxation time was extrapolated from the decay in signal intensity with increasing echo times for a given image slice and displayed as the relaxation rate R2*, the inverse of the relaxation time T2* (Fig. 1A). ROIs were manually drawn on a reference image of the cross-sections of each phantom tube to include all pixels without visible susceptibility artifacts. R2* values for each phantom concentration were calculated by linear regression of the log-transformed average ROI signal for each slice. For each tube, the slice with the highest R^2 (goodness of fit) was selected for plotting the linear relationship between $R_2^* = 1/T_2^*$ and FMX concentrations (Fig. 1B) as given in Eq. 1, with $R2^*_0$ representing the intrinsic relaxation rate of plasma without FMX and r2* representing a relaxivity constant. Plasma control samples into which a known amount of FMX had been added served as

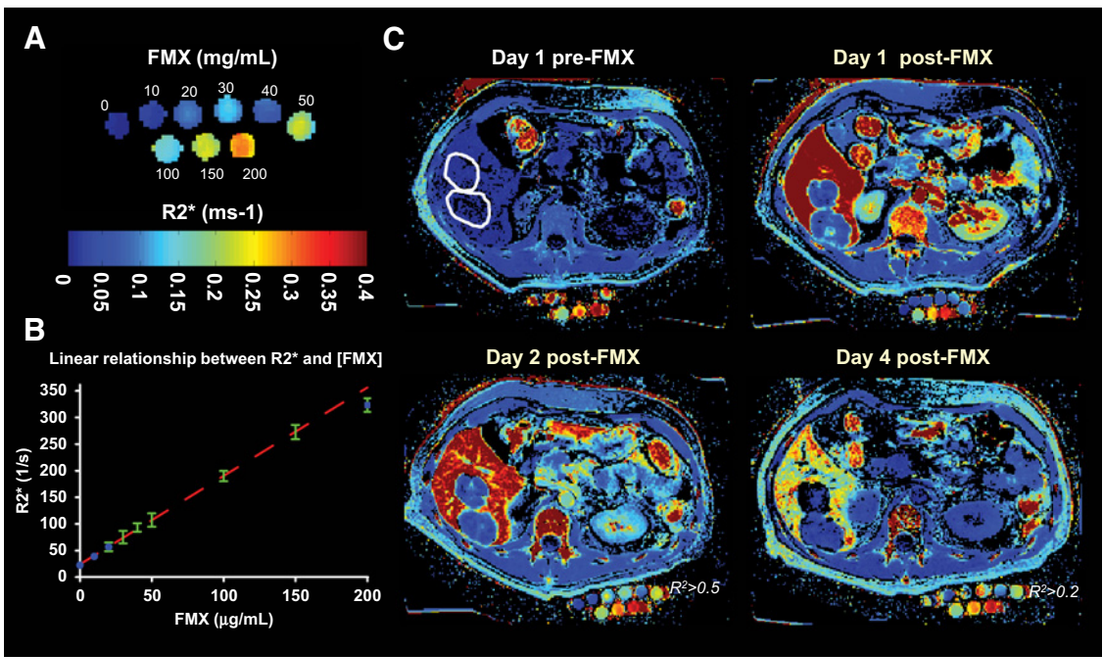

Figure 1.

FMX distribution kinetics assessed by MRI R2* maps. **A,** Enlarged view of the FMX phantom, with tubes containing FMX concentrations from 0–200 μg/mL. A pixel-by-pixel view of R2* is shown for illustration purposes only, as R2* values for each phantom concentration were actually calculated by linear regression of the log-transformed mean ROI signal for each slice. **B,** Linearity of relationship between FMX concentration and the relaxation rate R2* across 37 measurements of the FMX phantom during plasma FMX measurements (mean ± SD). The 200-μg/mL FMX tube was not included in the trend line. **C,** Representative pseudocolored relaxometric R2* maps derived from patient images before FMX dosing, immediately after (1–2 hours), 24 hours, and 72 hours after dosing with 5 mg/kg FMX. Approximate lesion locations are indicated by dashed lines in the image before FMX dosing.

additional process validation (not shown).

$$R2^* = R2_0^* + r2^* \times [FMX] \quad (1)$$

Similarly, FMX concentrations in lesions, tissues, or other regions of interest were extrapolated from the pre- and postinjection relaxation rates using the nominal relationship observed for the FMX phantom [Eq. 2].

$$[FMX] = \frac{\left(R2^*_{post} - R2^*_{0,post}\right)}{r2^*} - \frac{\left(R2^*_{pre} - R2^*_{0,pre}\right)}{r2^*} \quad (2)$$

$FMX_{0\rightarrow 72}$ tumor exposure parameters were estimated from FMX values derived from MRI using a simple linear piecewise function (33). We made the assumption that the difference in the contribution of local field inhomogeneities to $R2^*$ on the different scan days (captured in the difference between $R2^*_{0,post}$ and $R2^*_{0,pre}$) is negligible relative to the change in $R2^*$ produced by FMX (captured in the difference between $R2^*_{post}$ and $R2^*_{pre}$).

Response analysis

Patient response assessment was performed by local investigators per RECIST 1.1. For further analysis of lesion responses in correlation to FMX-MRI, a central radiology review was performed in a blinded, independent manner. Details regarding central radiology review can be found in Supplementary Materials.

Plasma and tumor pharmacokinetic modeling of FMX

Pharmacokinetic profiles of FMX in plasma were described by a one-compartment model, which was then connected to the tumor pharmacokinetic model with tumor capillary and tissue compartments (Fig. 2A; Supplementary Information). As the volume of distribution for FMX (Supplementary Table S2) suggests a low transvascular flux compared with small-molecule contrast agents, it was assumed that FMX transport to the tumor tissue compartment is permeability limited. The levels of FMX in tumor capillary thus correspond to the central blood compartment, hence making the volume transfer constant K^{trans} equal to the inward permeability surface area product, PeS_{in} (34). The tissue deposition of FMX depends on tissue

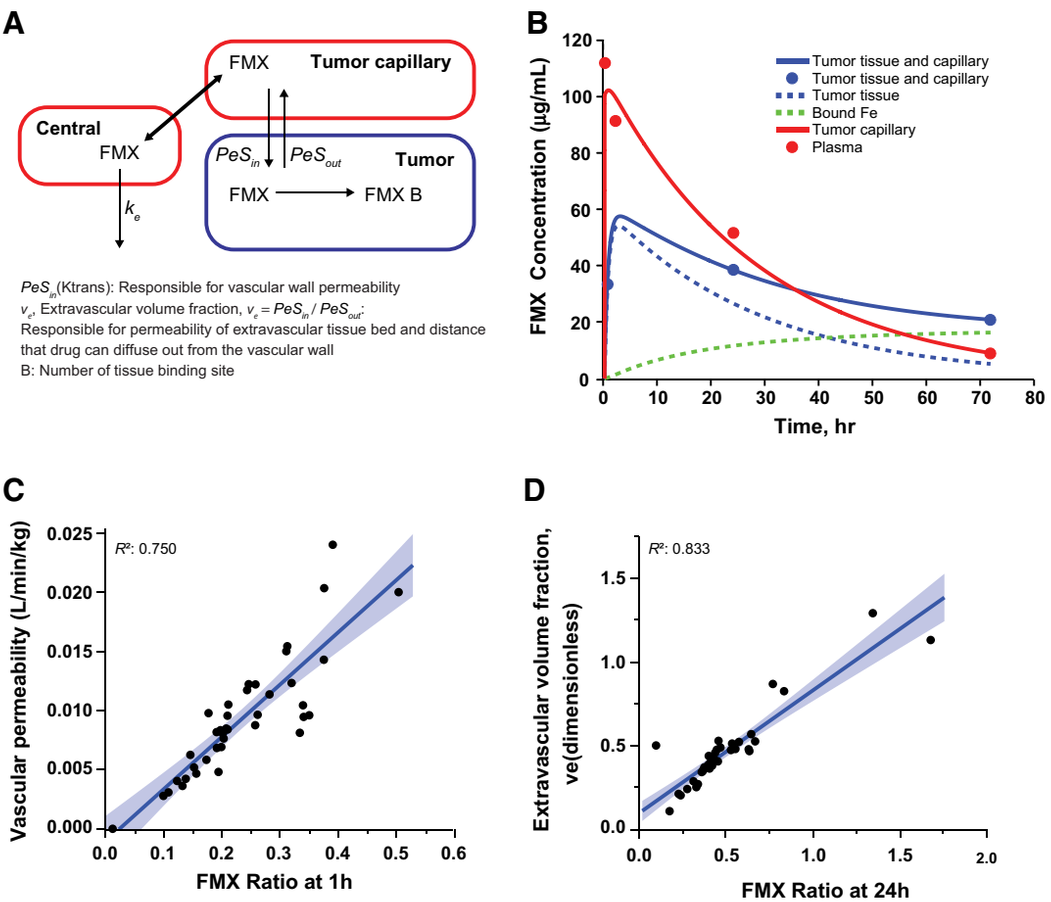

Figure 2.

Pharmacokinetic model of FMX. **A,** Schematic of multicompartment model for FMX distribution between plasma, tumor capillaries, and tumor compartments. Retention of FMX in the tumor compartment is mimicked by tissue binding sites. **B,** Mechanistic pharmacokinetic model for tumor deposition of FMX driven by permeability and binding parameters; an example of lesion fits for high-permeability/high-signal retention is shown. **C** and **D,** Permeability-based parameters for tumor deposition in pharmacokinetic model correlate strongly with FMX signal measured at 1 hour (PeS_{in}; **C**) and 24 hours (**D**; PeS_{in}/PeS_{out}). The normalized FMX ratio between tumor and plasma values is shown to account for plasma FMX pharmacokinetic variability.

permeability (PeS_{in} or K^{trans}) and extravascular volume fraction (v_e). In the tumor tissue compartment, it is assumed that FMX can also bind to the tissue-binding sites (B), which is intended to capture macrophage uptake of FMX (Fig. 2A). Model equations and additional information are summarized in Supplementary Information. Estimated model parameters are summarized in Supplementary Table S3.

Statistical analysis

Pearson pairwise correlation analysis was performed between FMX levels, lesion size changes, and pharmacokinetic model parameter. Spearman rank correlation analysis was performed between individual lesion averages of irinotecan levels and the patient's time on treatment. One-way ANOVA was used to assess the relationship between lesion size change and FMX groups below and above the median. ROC for lesion classification were calculated by using two different thresholds for lesion size change to define responding patients; either lesion shrinkage (any decrease from baseline) or partial response (≥30% decrease from baseline). All statistical analyses were implemented in JMP v11 (SAS).

See Supplementary information for additional Materials and Methods.

Results

Clinical observations

Between December 12, 2012 and March 3, 2014, 21 patients with metastatic solid tumors were screened, of whom 15 met eligibility criteria and enrolled on the FMX-MRI portion of the protocol. Data acquisition for image analysis was successfully completed in all but two patients. Thirteen patients continued to nal-IRI treatment and received between 1 and 31 doses (median, 4 doses). Patient demographics are given in Table 1. On average, patients received 95% of the intended dose. Nine (69%) patients underwent FMX imaging, biopsy collection, nal-IRI treatment, and at least one posttreatment CT scan for RECIST response assessment and were therefore evaluable for detailed analyses of FMX deposition characteristics and tumor lesion responses, while 4 patients discontinued nal-IRI without acquisition of a scan because of clinical deterioration and/or serious adverse events. We observed 1 partial response (breast cancer), 5 stable disease, and 5 progressive disease responses; 2 patients were not clinically evaluated. Median time on treatment was 57 days (range, 29–434 days), with 4 patients [breast (2), duodenal, and mesothelioma] on treatment for >110 days.

Table 1. Demographic and baseline characteristics

	FMX $n = 15$	nal-IRI $n = 13$
Age, years, median (range)	60 (28–80)	58 (28–80)
Sex, *n* (%)		
Male	4 (27)	4 (31)
Female	11 (73)	9 (69)
Race, *n* (%)		
White	14 (93)	12 (92)
American-Indian/American-Native	1 (7)	1 (8)
ECOG, *n* (%)		
0	7 (47)	7 (54)
1	8 (53)	6 (46)
Prior lines of therapy, median (range)	4 (1–10)	4 (1–10)

No adverse effects such as hypersensitivity, other allergic reactions, or dizziness were observed during the FMX administration and during a 30-minute observation phase before the first post-injection MRI. Adverse events with nal-IRI were consistent with those previously reported, including diarrhea, nausea, vomiting, and neutropenia (11, 35).

FMX-MRI imaging and quantitation

Calibration curves for the dependence of R2* on FMX concentration yielded consistent values, with an average r2* relaxivity of 1.661 mL/s/μg (92.8 1/s/mmol/L) (Fig. 1B). The R2* values for the 150-μg/mL FMX phantom tube were comparable with the maximally observed R2* values in either plasma or tissues.

Baseline relaxation rates were 21.8 ± 12.8/s, 33.5 ± 17.6/s, 39.0 ± 42.0/s, and 28.4 ± 3.1/s for tumor lesions, liver, spleen, and muscle, respectively. FMX led to rapid R2* increases in the blood, liver, and spleen (Fig. 1C). FMX accumulation in tumor lesions was detectable and heterogeneous within lesions, but generally at levels lower than the liver and spleen. Liver lesions were also well demarcated from the surrounding tissue in the presence of FMX (see Supplementary Fig. S2A as example). The R2* signal had not returned to baseline in select tissues and most tumor lesions at 72 hours (Fig. 1C, day 4 following FMX). For lesions evaluated by FMX-MRI, lesion sizes at baseline measured on average 32.1 ± 15.62 mm in diameter. No correlations between lesion sizes and uptake were observed.

FMX levels in background tissues or tumor lesions ($n = 46$) were calculated on the basis of phantom measurements. Maximal tumor lesion FMX concentrations were observed at the 1- or 24-hour imaging time points after FMX injection (Fig. 3A). Median (with median absolute deviation) FMX levels for all measured lesions were 32.7 (6.2) μg/mL measured at 1 hour after FMX injection, 34.5 (10.4) μg/mL after 24 hours, and 11.4 (4.5) μg/mL after 72 hours. Lesion uptake for individual patients is shown in Fig. 3B. Heterogeneity of uptake across lesions was observed within patients as well as across patients. Lesion levels reached 2.5%–30% of the injected dose per kilogram of tissue at 24 hours. The 24-hour FMX levels correlated linearly with overall FMX exposure AUC_{0-72h} ($R^2 = 0.9502$; slope 95% CI, 42.9–49.4); exposures differed by 8.3× between all imaged lesions, while interlesional ranges of 1.03× to 4.22× were observed for individual patients. Intralesion heterogeneity showed median exposure differences of 1.56×, although >10× higher differences were also observed.

FMX uptake was minimal in normal muscle, a tissue with small endothelial fenestrations, and returned to baseline levels within 72 hours (Fig. 3C). In liver and spleen, the FMX concentration was initially comparable with plasma levels at 0.5–2 hours, but the FMX concentration decreased much more rapidly in plasma than in these tissues. After 72 hours, FMX levels in liver and spleen were 6× and 4× higher, respectively, than in plasma. In plasma, the elimination half-life of FMX was 22.1 hours ($n = 14$; 95% CI, 19.7–24.5; Fig. 3C), consistent with previously published data in healthy subjects (36, 37) and comparable with the reported half-life of nal-IRI (11, 35). Plasma exposure ($AUC_{0\rightarrow t}$) for FMX and nal-IRI were correlated ($r = 0.7528$; $P = 0.0030$). Other pharmacokinetic parameters for FMX are summarized in Supplementary Table S2. Metabolic turnover of FMX resulted in elevated plasma ferritin levels as described previously (29, 36). Ferritin

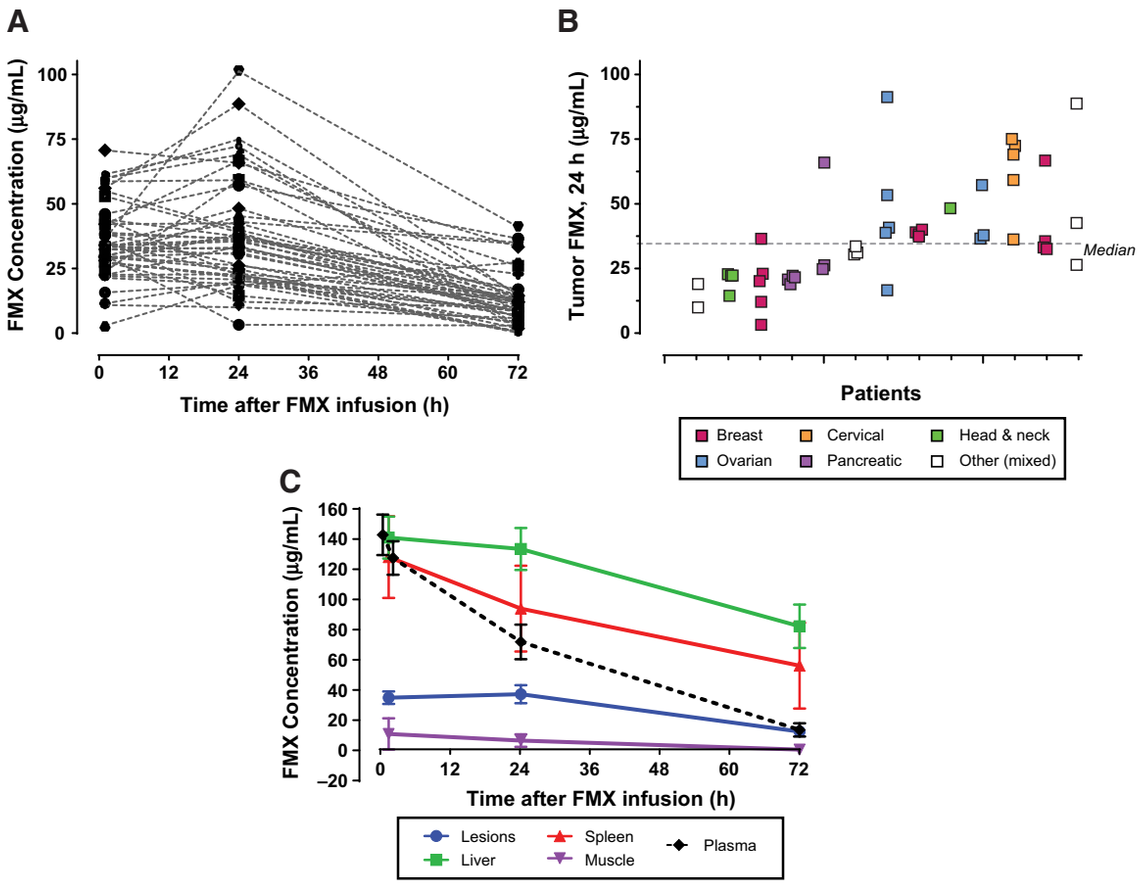

Figure 3.

FMX concentration in lesions. **A,** Time-course of FMX concentration in tumor lesions 1 hour, 24 hours, and 72 hours after FMX injection. **B,** Extrapolated tumor FMX concentrations per individual patient data at 24 hours. **C,** Average FMX kinetics in tumor lesions ($n = 46$) and comparison with liver and spleen clearance organs ($n = 11$) and normal tissue ($n = 13$) as well as plasma pharmacokinetics ($n = 14$). Error bars, 95%CI.

levels in plasma increased from a median concentration of 267 ng/mL (range, 45–1,481 ng/mL) during patient screening to 691 ng/mL (range, 430–1,730 ng/mL) at day 4 after FMX injection. One month later, levels declined to the previously observed baseline with median concentrations of 238 ng/mL (range, 115–775 ng/mL).

Pharmacokinetic modeling of FMX

The multicompartmental pharmacokinetic model described lesion-specific data well, with the exception of a single patient, and captured signal characteristics from regions of interest for either whole lesions or lesion subregions chosen to represent areas of high permeability/high retention (Fig. 2B) or low permeability/low retention (Supplementary Fig. S3A). The FMX lesion values measured at 1 hour following injection correlated best with the permeability parameter (PS_{in} or K^{trans}) with $R^2 = 0.750$ (Fig. 2C). The extravascular volume fraction (ratio between the inward and outward permeability-surface products) correlated best with FMX lesion values measured at 24 hours following injection ($R^2 = 0.833$; Fig. 2D). In contrast, permeability-related parameters did not correlate with FMX lesion values measured after 72 hours. However, the tissue binding site parameter contributed weakly to the FMX lesion levels at 72 hours ($R^2 = 0.423$; Supplementary Fig. S3B) but showed no correlation ($R^2 = 0.000$) to the 1-hour and 24-hour FMX lesion signals. The estimated K^{trans} values of FMX, averaged for each of the 13 evaluable patients, were greater than those of liposomes, consistent with the expectation of greater permeability of the smaller FMX nanoparticle relative to nal-IRI (18, 38).

FMX distribution and irinotecan levels in biopsies

Staining of serial tumor sections demonstrated deposition of FMX in macrophage-rich regions of vascular-accessible stromal areas located around tumor nests (Fig. 4A). This was particularly evident in liver lesions in which the regular pattern of Kupffer cells was replaced by a higher density of CD68-positive cells in the stromal area around tumor nests. Prussian blue staining of iron was seen in Kupffer cells, which provides an indirect assessment of FMX deposition. The strongest staining overlapped with accumulation of CD68-positive cells in stromal areas (Fig. 4B; Supplementary Fig. S4). Prussian blue signals were observed in biopsies at both 72 hours and 168 hours after FMX administration.

Irinotecan levels, averaged from 2 separate biopsy locations in the same tumor lesion, showed a statistically nonsignificant correlation to the corresponding permeability associated FMX signals at 1 hour (Fig. 4C) and 24 hours (Fig. 4D), respectively

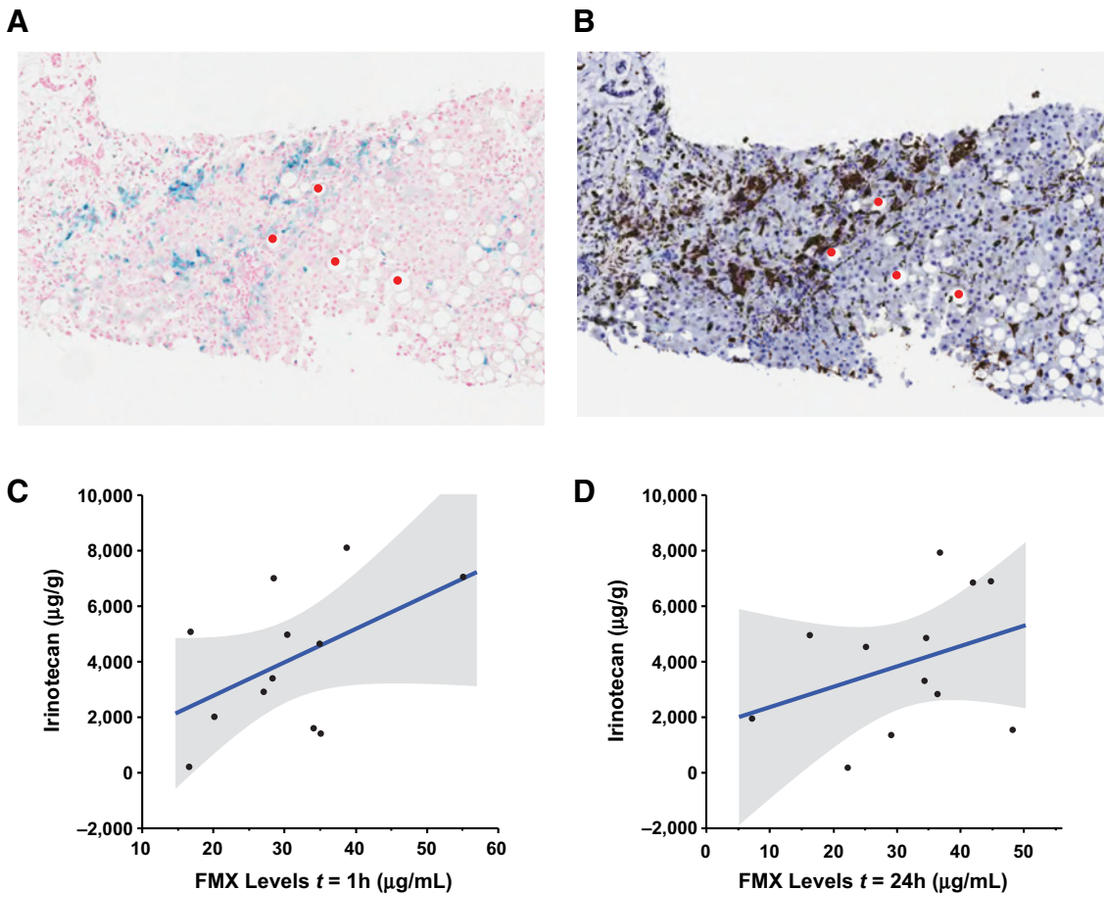

Figure 4.

Macrophage and iron staining in tumor biopsies. **A** and **B,** Serial tumor sections from FFPE biopsies of liver lesions were stained for FMX (Prussian blue; **A**) and macrophages (CD68; **B**). FMX deposition is detectable primarily in vascular-accessible macrophages in stromal areas surrounding tumor lesions. **C** and **D,** Relationship between lesion FMX concentrations measured at 1 hour (**C**) or 24 hours (**D**) with the average irinotecan concentrations measured in the biopsies.

[Spearman $\rho = 0.4266$ ($P = 0.1667$) at 1 hour; 0.3706 ($P = 0.2356$) at 24 hours; 0.1608 ($P = 0.6175$) at 72 hours]. Irinotecan levels in biopsies showed median differences of 2.22× (range, 1.01–9.06; $n = 13$) between different biopsy locations for each patient, and 2.29× differences (range, 1.10–5.71; $n = 6$) for consecutive passes in the same lesion. Average biopsy pass levels of irinotecan in tumor lesions represented 0.14%–6.07% of the injected dose of nal-IRI per kilogram of tissue at 72 hours and were 21.1% lower than the corresponding plasma levels.

Lesion response

Lesion averages of irinotecan levels showed a strong and significant correlation to the time on treatment for each patient (Supplementary Fig. S5; Spearman's $\rho = 0.7824$, $P = 0.0016$). There was also a positive trend between FMX lesion values and irinotecan levels. We therefore evaluated if FMX lesion values also correlated with response characteristics at the lesion level.

Response assessments from CT imaging (see Supplementary Fig. S2B as example) were available from 9 patients for at least 1 evaluation at 8 weeks after the start of treatment. For 4 patients more than 1 assessment was available. Six of 33 lesions were classified as responders as assessed by a decrease of the longest diameter of 30% or more, and 10 lesions were classified as responders as assessed by volume decreases of 50% or more. Fourteen lesions (42%) had decreased in diameter during at least 1 assessment interval. CT image density changes did not correlate with changes in diameter or volume of lesions.

For the subset of CT-evaluable lesions for which FMX-MRI was available ($n = 31$), the median FMX levels were 34.1 µg/mL measured approximately 1 hour after FMX injection, 33.6 µg/mL after 24 hours, and 9.8 µg/mL after 72 hours. Individual lesions were classified on the basis of FMX levels as either below or above the median of all lesion values at that time point. FMX levels at 1 hour (Fig. 5A) and 24 hours (Fig. 5B) after FMX injection were significantly associated with better lesion responses as measured by best change in lesion size ($P < 0.0001$ at 1 hour; $P < 0.003$ at 24 hours); no relationship was observed at 72 hours ($P = 0.83$; data not shown). Lesion responses measured at the earliest available posttreatment CT imaging at 8 weeks showed a similar statistical significance for this association ($P = 0.0001$ at 1 hour; $P < 0.003$ at 24 hours; data not shown). Receiver operating characteristics for lesion classification according to 2 separate thresholds for lesion size reduction, namely lesion shrinkage (best lesion size change

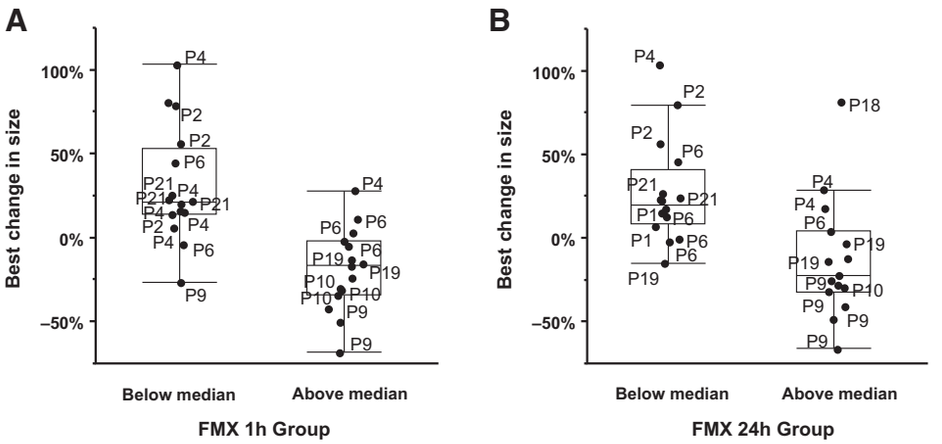

Figure 5.
FMX signal in lesion correlates with lesion size change. FMX signals at 1 hour (**A**) or 24 hours (**B**) are grouped relative to the median value observed in the evaluable lesions (9 patients, 31 lesions) and compared with the best change in lesion size seen with RECIST CT.

<0%) and partial response (best lesion size change ←30%), had an AUC ≥0.8 for early FMX measurements (i.e., 1 hour and 24 hours; Supplementary Fig. S6). This classification approach also performed slightly better with data from the 1-hour time point that correlated best with the inward permeability-surface product (PS_{in} or K^{trans}) parameter of FMX.

Discussion

This study provides a first clinical evaluation of using noninvasive imaging of a potential nanodiagnostic to evaluate lesion permeability characteristics as a surrogate measure for the effectiveness of a subsequently dosed nanotherapeutic. In particular, we demonstrate the feasibility of an MRI method using the superparamagnetic iron oxide particle FMX to quantitatively assess tumor permeability properties in patients and relate it with lesion response to treatment with nal-IRI. Our results indicate that lesion FMX measurements at up to 24 hours strongly correlated with lesion-specific permeability parameters from a FMX mechanistic pharmacokinetic model. Lesion FMX levels at 72 hours correlated more with late binding events, likely corresponding to the observed Prussian blue staining overlapping with CD68 signals in stromal areas of tumor biopsies. This FMX-based evaluation can be implemented with a minimum of 2 imaging sessions, and its timing can be selected to emphasize distinct lesion characteristics of interest depending on the nanotherapeutic under investigation.

We analyzed the relationship between FMX levels in tumor lesions and nal-IRI activity, and found a statistically significant correlation between changes in lesion diameters and lesion-specific uptake of FMX at 1 and 24 hours after FMX administration. This suggests that lesion permeability to FMX may be a useful biomarker for tumor response to nal-IRI in patients with solid tumors and also indicates that EPR-driven initial deposition effects may correlate across different nanoparticle types. FMX and nal-IRI both displayed extended plasma circulation and are thought to share plasma clearance mechanisms such as interaction with the monocyte phagocytic system. Although patient-specific differences in the interaction of plasma proteins with these nanoparticles (39) may add confounding factors, this feasibility study was not powered to evaluate the effect of patient covariates, including ethnicity, sex, and age. Our results were based on data obtained from a small number of patients with multiple cancer types. If this relationship holds true in a larger population, it would suggest that deposition may be a dominant factor for response to nal-IRI in certain tumor types. The importance of lesion permeability for liposomal delivery has been shown in preclinical tumor models (15, 16).

We had also hypothesized that imaging of macrophage levels in tumor lesions may yield information about the drug retention of nal-IRI and associated drug conversion activities. This hypothesis was based on observations in preclinical models (25) that showed broad colocalization of FMX with liposomes in perivascular stromal areas as well as enrichment of both liposomes and FMX in host cells such as tumor-associated macrophages (TAM). For example, experiments in murine syngeneic or xenogeneic models have demonstrated that myeloid cells, particularly TAMs, accumulate the largest share (78%–94% depending on tumor model at 24 hours) of nal-IRI (40). Miller and colleagues (27) noted similar patterns of colocalization and predominant accumulation of FMX and nanoparticles in host cells, driven by the comparable extended circulating half-life of both nanoparticles and the EPR effect. Both nanoparticles take advantage of overlapping microvascular accessibility, even if deposition kinetics for FMX are faster and the distribution of the two nanoparticles within the perivascular space of the tumor can be more divergent on the cellular level. Notably, colocalization of FMX and a therapeutic nanoparticle improved at the lower spatial resolution found in clinical MRI (27). A surprising observation in this study is that late binding events identifiable by FMX-MRI at 72 hours did not correlate with lesion response in patients treated with nal-IRI. This is reminiscent of a previous report (26) in which liposomal deposition into tumors was shown to be independent of liposomal binding characteristics, whereas subsequent intratumoral biodistribution and cellular retention was affected. FMX measurements at 72 hours also had a lower signal-to-noise ratio, thus making stratification more difficult at that time point. For clinical evaluation of binding events by FMX-MRI, imaging times between 24 and 72 hours may have to be explored.

Miller and colleagues (27) had suggested that when payload release from a nanocarrier is more rapid, its intratumoral distribution may be more dependent on vascular permeability and extracellular volume fraction. Nanoliposomal carriers are thought to release their payload either interstitially, possibly modulated by ammonia levels (41), or from cells after liposomal uptake and intracellular processing by target cells following ligand-mediated endocytosis or phagocytic cells such as macrophages in the case of passively-targeted liposomes such as nal-IRI (2, 4). In addition,

cellular release is likely to be affected by payload and/or metabolite physicochemical properties, including their polar surface area or interaction with cellular components. Preclinical results with nal-IRI indicated that bioavailability of the liposomal payload is likely not restricted to TAMs. Although liposomal deposition is nonuniform and perivascular, primarily in stromal areas, γH2AX staining at 24–72 hours after liposome dosing in a pancreatic orthotopic model was broadly seen across all tumor areas but not the stroma (42). Nanoliposomal carriers may thus exhibit comparably faster drug release rates than therapeutic nanoparticles with a more erosive, slower release mechanism (27, 43), which could possibly explain the lack of correlation between lesion response to nal-IRI and late binding events of FMX in this study.

R2 and R2* mapping are accepted clinical tools for evaluating tissue iron concentrations, both for iron overload disorders (44, 45) and for tracking of ultrasmall superparamagnetic iron oxide particles (18, 24, 46). To enable accurate lesion FMX assessments, baseline MRI signals were subtracted from later time points, and FMX phantom reference was used with all scans. Our R2* values for reference tissues at baseline and at 72 hours compared well with published values (44), despite differences in MRI acquisition parameters such as flip angle, repetition time, and slice thickness. The metabolism of FMX and compartmentalization within cells are potential confounding factors that may influence accurate quantitation of FMX levels in tumor lesions. Findings by Storey and colleagues (44) suggest that the magnetite core of FMX remains largely intact over 72 hours, the time scale of our study. Therefore, FMX metabolism is not expected to greatly influence measurements with tumor lesions. FMX degradation (44, 47) will result in a corresponding decrease in the R2* signal, as the magnetic moment of ferritin is far smaller than that of FMX. Compartmentalization of iron oxide particles after phagocytic uptake into macrophages can double R2* (48, 49) and may thus counteract any loss of signal due to partial degradation of FMX particles during the imaging period (36, 44, 47). The effects of compartmentalization may also lead to an overestimation of FMX levels particularly at late time points, although this error contribution is thought to be relatively uniform across a patient population. Subtraction of baseline MRI signal proved to be important: baseline R2* values were variable, and the correlation with response to nal-IRI was not significant without correcting for baseline signal in this patient population. Inclusion of a FMX phantom reference allowed transformation of R2* values to FMX concentrations and also served as an MRI quality control. Furthermore, the inclusion of a phantom reference is potentially important for expanding to multiple sites and MRI scanners that have capabilities of acquiring T2* sensitive sequences by a variety of methods including FSPGR acquisition series and multiecho multislice gradient-echo (mGRE) sequences. The now recommended extended infusion schedule of FMX (29) is not expected to affect current strategies of image data analysis because the duration of administration is still small relative to the extended half-life and, thus, deposition time frame of FMX.

Lesion response is dependent not only on sufficient deposition and distribution of the payload but also on appropriate conversion to SN-38 and chemosensitivity of tumor cells, confounding factors adding to response variability in patients and not interrogated with this FMX imaging approach. This study did not address whether treatment with nal-IRI may potentially modify delivery characteristics for later treatment cycles. However, initial response characteristics of tumor lesions appear sufficiently representative of the overall treatment response in the current study. We observed a strong and significant correlation between average irinotecan levels in lesions and the time on treatment for each patient. Furthermore, the concentrations of irinotecan measured in biopsies at 72 hours after administration of nal-IRI were far higher than could be accounted for by microcirculatory levels for total irinotecan and its liposomal encapsulation (15, 50), consistent with intratumoral deposition of nal-IRI. The composition of nal-IRI precluded any direct IHC-based analysis of the liposomal distribution in post-treatment FFPE samples from our patients. Preclinical findings (15) had suggested that irinotecan levels at 72 hours may be used as a surrogate measure for nal-IRI permeability. The limited correlation between irinotecan and FMX levels in tumor biopsies is likely due to the fact that biopsy location and region selection on MRI and CT images could only be approximated in this study and that the biopsy needle with an inner diameter of 0.838 mm was 1/7th of the MRI slice thickness. Punch biopsies may be better suited for evaluating liposome and FMX deposition, but this is only amenable to a surgical setting.

This study demonstrated that the EPR effect, as measured by FMX-MRI, is highly variable in a diverse patient cohort with solid tumors. Furthermore, variability was observed not only across patients, but also across individual lesions within a patient. The observation that FMX delivery correlated with response to treatment with nal-IRI at the lesion level suggests the potential significance of this finding. However, individual lesion responses may not directly translate into patient-specific outcomes, and the integration of permeability characteristics across multiple patient lesions requires further investigation. Presumably, sufficient delivery is required to most, if not all, lesions within a patient to successfully treat disease. This variability highlights a key challenge in successful therapy with nanotherapeutic agents. FMX-MRI is a promising, novel noninvasive biomarker that may predict responsiveness to therapeutic nanoparticles in general and nal-IRI therapy as indicated in this study. Further development using this approach continues in the expansion phase of a study in patients with metastatic breast cancer (31).

Disclosure of Potential Conflicts of Interest

R. Korn is a consultant/advisory board member for ImaginAB. J.C. Sachdev reports receiving commercial research grants from Celgene and Pfizer Inc. and is a consultant/advisory board member for Celgene. D.C. Drummond and J.B. Fitzgerald hold ownership interest (including patents) in Merrimack Pharmaceuticals. No potential conflicts of interest were disclosed by the other authors.

Authors' Contributions

Conception and design: R.K. Ramanathan, R. Korn, S.G. Klinz, D.C. Drummond, E. Bayever, J.B. Fitzgerald

Development of methodology: R.K. Ramanathan, R. Korn, N. Raghunand, J. Prey, S.G. Klinz, J. Kim, E. Bayever

Acquisition of data (provided animals, acquired and managed patients, provided facilities, etc.): R.K. Ramanathan, R. Korn, J.C. Sachdev, R.G. Newbold, G. Jameson, J. Cain, E. Bayever

Analysis and interpretation of data (e.g., statistical analysis, biostatistics, computational analysis): R.K. Ramanathan, R. Korn, N. Raghunand, J.C. Sachdev, G.J. Fetterly, S.G. Klinz, J. Kim, J. Cain, B.S. Hendriks, E. Bayever, J.B. Fitzgerald

Writing, review, and/or revision of the manuscript: R.K. Ramanathan, R. Korn, N. Raghunand, J.C. Sachdev, G. Jameson, G.J. Fetterly, S.G. Klinz, J. Kim, J. Cain, B.S. Hendriks, D.C. Drummond, E. Bayever, J.B. Fitzgerald

Administrative, technical, or material support (i.e., reporting or organizing data, constructing databases): J. Kim

Study supervision: R.K. Ramanathan, E. Bayever, J.B. Fitzgerald

Acknowledgments

We thank the patients and their families for their incredible help. We thank Daniel D. Von Hoff for his support of nal-IRI and his interest in this study. We thank all clinical staff who assisted with the study, especially Katie Marceau, Vickie Marsh, and Sam Ejadi, of the Virginia G Piper Cancer Center, Scottsdale, Arizona, and radiologists John M. Neil and Gavin P. Slethaug, of Imaging Endpoints. Brynne Crowell, Linda Vocila, and Linda Bavisotto of TGen Drug Development provided study support. Kimberly Clark, of Roswell Park Cancer Institute, Buffalo, New York, supported the biopsy metabolite studies. Among the supporting staff at Merrimack Pharmaceuticals, Aurelie Bouzelmat and Sarah Blanchette managed the study, Jon Taie and Victor Moyo provided additional study support, and Ashish Kalra, Nancy Paz, Helen Lee, Omid Ghasemi, and Walid Kamoun participated in reviews, brainstorming, and discussions. We thank Ulrik B. Nielsen for his vision and support of nal-IRI and this study. Editorial assistance was provided by Payal Gandhi of ApotheCom.

Grant Support

This work was supported by Merrimack Pharmaceuticals, Inc. The LC/MS-MS analysis was conducted by the Bioanalytics, Metabolomics and Pharmacokinetics (BMPK) Shared Resource of Roswell Park Cancer Institute, which is partially supported by National Cancer Institute (NCI) grant P30CA016056.

The costs of publication of this article were defrayed in part by the payment of page charges. This article must therefore be hereby marked *advertisement* in accordance with 18 U.S.C. Section 1734 solely to indicate this fact.

Received August 11, 2016; revised January 19, 2017; accepted January 20, 2017; published OnlineFirst February 3, 2017.

References

1. Drummond DC, Meyer O, Hong K, Kirpotin DB, Papahadjopoulos D. Optimizing liposomes for delivery of chemotherapeutic agents to solid tumors. Pharmacol Rev 1999;51:691–743.
2. Drummond DC, Noble CO, Hayes ME, Park JW, Kirpotin DB. Pharmacokinetics and in vivo drug release rates in liposomal nanocarrier development. J Pharm Sci 2008;97:4696–740
3. Maeda H, Wu J, Sawa T, Matsumura Y, Hori K. Tumor vascular permeability and the EPR effect in macromolecular therapeutics: a review. J Control Release 2000;65:271–84.
4. Bertrand N, Wu J, Xu X, Kamaly N, Farokhzad OC. Cancer nanotechnology: the impact of passive and active targeting in the era of modern cancer biology. Adv Drug Deliv Rev 2013;66:2–25.
5. Harrington KJ, Mohammadtaghi S, Uster PS, Glass D, Peters AM, Vile RG, et al. Effective targeting of solid tumors in patients with locally advanced cancers by radiolabeled pegylated liposomes. Clin Cancer Res 2001;7:243–54.
6. Hobbs SK, Monsky WL, Yuan F, Roberts WG, Griffith L, Torchilin VP, et al. Regulation of transport pathways in tumor vessels: role of tumor type and microenvironment. Proc Natl Acad Sci U S A 1998;95:4607–12.
7. Lammers T, Rizzo LY, Storm G, Kiessling F. Personalized nanomedicine. Clin Cancer Res 2012;18:4889–94.
8. Baetke SC, Lammers T, Kiessling F. Applications of nanoparticles for diagnosis and therapy of cancer. Br J Radiol 2015;88:20150207.
9. Shields AF, Siegel BA, Miller KD, Munster PN, Ma C, Lee H, et al. Quantification of 64Cu-MM-302 liposome biodistribution and lesion deposition kinetics using PET/CT imaging in advanced breast cancer patients. WMIC 2014;19–SS 109.
10. Drummond DC, Noble CO, Guo Z, Hong K, Park JW, Kirpotin DB. Development of a highly active nanoliposomal irinotecan using a novel intraliposomal stabilization strategy. Cancer Res 2006;66:3271–7.
11. Onivyde [package insert]. Cambridge, MA: Merrimack Pharmaceuticals, Inc; 2015.
12. Wang-Gillam A, Li C, Bodoky G, Dean A, Shan YS, Jameson G, et al. Nanoliposomal irinotecan with fluorouracil and folinic acid in metastatic pancreatic cancer after previous gemcitabine-based therapy (NAPOLI-1): a global , randomised , open-label , phase 3 trial. Lancet 2016;387:545–57.
13. Pommier Y. Topoisomerase I inhibitors: camptothecins and beyond. Nat Rev Cancer 2006;6:789–802.
14. Chabot GG. Clinical pharmacokinetics of irinotecan. Clin Pharmacokinet 1997;33:245–59.
15. Kalra AV, Kim J, Klinz SG, Paz N, Cain J, Drummond DC, et al. Preclinical activity of nanoliposomal irinotecan is governed by tumor deposition and intratumor pro-drug conversion. Cancer Res 2014;74:7003–13.
16. Hendriks BS, Reynolds JG, Klinz SG, Geretti E, Lee H, Leonard SC, et al. Multiscale kinetic modeling of liposomal doxorubicin delivery quantifies the role of tumor and drug-specific parameters in local delivery to tumors. CPT Pharmacometrics Syst Pharmacol 2012;1:e15.
17. Karathanasis E, Chan L, Karumbaiah L, McNeeley K, D'Orsi CJ, Annapragada AV, et al. Tumor vascular permeability to a nanoprobe correlates to tumor-specific expression levels of angiogenic markers. PLoS One 2009;4:e5843.
18. Daldrup-Link HE, Shames DM, Wendland M, Okuhata Y, Link TM, Rosenau W, et al. Correlation of dynamic contrast-enhanced magnetic resonance imaging with histologic tumor grade: comparison of macromolecular and small-molecular contrast media. Pediatr Radiol 1998;28:67–78.
19. Turetschek K, Preda A, Novikov V, Brasch RC, Weinmann HJ, Wunderbaldinger P, et al. Tumor microvascular changes in antiangiogenic treatment: Assessment by magnetic resonance contrast media of different molecular weights. J Magn Reson Imaging 2004;20:138–44.
20. Jensen GM, Bunch TH. Conventional liposome performance and evaluation: lessons from the development of Vescan. J Liposome Res 2007;17:121–37.
21. Lee H, Zheng J, Gaddy D, Orcutt KD, Leonard S, Geretti E, et al. A gradient-loadable ^{64}Cu-chelator for quantifying tumor deposition kinetics of nanoliposomal therapeutics by positron emission tomography. Nanomedicine 2015;11:155–65.
22. Izaguirre EW, Sun M, Drummond DC, Kirpotin DB, Funk T, Thompson S, et al. SPECT-CT study of directed drug delivery using In-111 labeled liposomes in a murine mammary carcinoma model. IEEE Nuclear Science Symposium Conference Record 2005;4:1965–8.
23. Neuwelt EA, Hamilton BE, Varallyay CG, Rooney WR, Edelman RD, Jacobs PM, et al. Ultrasmall superparamagnetic iron oxides (USPIOs): a future alternative magnetic resonance (MR) contrast agent for patients at risk for nephrogenic systemic fibrosis (NSF)? Kidney Int 2009;75:465–74.
24. Hamilton BE, Nesbit GM, Dosa E, Gahramanov S, Rooney B, Nesbit EG, et al. Comparative analysis of ferumoxytol and gadoteridol enhancement using T1- and T2-weighted MRI in neuroimaging. AJR Am J Roentgenol 2011;197:981–8.
25. Kalra A, Spernyak J, Kim J, Kamoun W, Sengooba A, Klinz SG, et al. Magnetic resonance imaging with an iron oxide nanoparticle demonstrates preclinically the feasibility of predicting intratumoral uptake and activity of MM-398 , a nanoliposomal irinotecan (nal-IRI). Cancer Res 2014;74(19 suppl):2065.
26. Kirpotin DB, Drummond DC, Shao Y, Shalaby MR, Hong K, Nielsen UB, et al. Antibody targeting of long-circulating lipidic nanoparticles does not increase tumor localization but does increase internalization in animal models. Cancer Res 2006;66:6732–40.
27. Miller MA, Gadde S, Pfirschke C, Engblom C, Sprachman MM, Kohler RH, et al. Predicting therapeutic nanomedicine efficacy using a companion magnetic resonance imaging nanoparticle. Sci Transl Med 2015;7:314ra183.
28. Pohlmann A, Karczewski P, Ku M-C, Dieringer B, Waiczies H, Wisbrun N, et al. Cerebral blood volume estimation by ferumoxytol-enhanced steady-state MRI at 9.4 T reveals microvascular impact of α1-adrenergic receptor antibodies. NMR Biomed 2014;27:1085–93.
29. Feraheme (ferumoxytol injection) [package insert]. Waltham, MA: AMAG Pharmaceuticals, Inc.; 2009–2015.
30. Daldrup-Link HE, Golovko D, Ruffel B, Denardo DG, Castaneda R, Ansari C, et al. MRI of Tumor-associated macrophages with clinically applicable iron oxide nanoparticles. Clin Cancer Res 2011;17:5695–704.

31. Merrimack Pharmaceuticals. Pilot study to determine biodistribution of MM-398 and feasibility of ferumoxytol as a tumor imaging agent. In: ClinicalTrials.gov [Internet]. Bethesda (MD): National Library of Medicine (US); 2000[cited 2016 Nov 01]. Available from: http://www.clinicaltrials.gov/ct2/show/NCT01770353.
32. Mitchell MD, Kundel HL, Axel L, Joseph PM. Agarose as a tissue equivalent phantom material for NMR imaging. Magn Reson Imaging 1986;4:263–6.
33. Koay EJ, Truty MJ, Cristini V, Thomas RM, Chen R, Chatterjee D, et al. Transport properties of pancreatic cancer describe gemcitabine delivery and response. J Clin Invest 2014;124:1525–36.
34. Miller JC, Pien HH, Sahani D, Sorensen AG, Thrall JH. Imaging angiogenesis: applications and potential for drug development. J Natl Cancer Inst 2005;97:172–87.
35. Roy AC, Park SR, Cunningham D, Kang YK, Chao Y, Chen LT, et al. A randomized phase II study of PEP02 (MM-398), irinotecan or docetaxel as a second-line therapy in patients with locally advanced or metastatic gastric or gastro-oesophageal junction adenocarcinoma. Ann Oncol 2013;24:1567–73.
36. Landry R, Jacobs PM, Davis R, Shenouda M, Bolton WK. Pharmacokinetic study of ferumoxytol: a new iron replacement therapy in normal subjects and hemodialysis patients. Am J Nephrol 2005;25:400–10.
37. Pai AB, Nielsen JC, Kausz A, Miller P, Owen JS. Plasma pharmacokinetics of two consecutive doses of ferumoxytol in healthy subjects. Clin Pharmacol Ther 2010;88:237–42.
38. Schmidt MM, Wittrup KD. A modeling analysis of the effects of molecular size and binding affinity on tumor targeting. Mol Cancer Ther 2009;8:2861–71.
39. Caracciolo G, Farokhzad OC, Mahmoudi M. Biological identity of nanoparticles in vivo: clinical implications of the protein corona. Trends Biotechnol. 2016Sep 20. [Epub ahead of print]
40. Kalra AV, Kim J, Klinz SG, Paz N, Reutt J, Patel J, et al. The tumor microenvironment modulates the delivery and activation of liposomal encapsulated irinotecan, MM-398. Cancer Res 2013;73(8 suppl):5622.
41. Silverman L, Barenholz Y. In vitro experiments showing enhanced release of doxorubicin from Doxil® in the presence of ammonia may explain drug release at tumor site. Nanomedicine 2015;11:1841–50.
42. Klinz S, Zheng J, De Souza R, Ventura M, Paz N, Hedley D, et al. Nanoliposomal irinotecan (nal-IRI) is an active treatment and reduces hypoxia as measured through longitudinal imaging using [18F] FAZA-PET in an orthotopic patient-derived tumorgraft model of pancreatic cancer. Poster #B47, presented at: Pancreatic Cancer: Advances in Science and Clinical Care; May 12–15, 2016; Orlando, FL.
43. Miller MA, Zheng Y-R, Gadde S, Pfirschke C, Zope H, Engblom C, et al. Tumour-associated macrophages act as a slow-release reservoir of nano-therapeutic Pt(IV) pro-drug. Nat Commun 2015;6:8692.
44. Storey P, Lim RP, Chandarana H, Rosenkrantz AB, Kim D, Stoffel DR, et al. MRI assessment of hepatic iron clearance rates after USPIO administration in healthy adults. Invest Radiol 2012;47:717–24.
45. Hernando D, Levin YS, Sirlin CB, Reeder SB. Quantification of liver iron with MRI: state of the art and remaining challenges. J Magn Reson Imaging 2014;29:997–1003.
46. Hedgire SS, Mino-Kenudson M, Elmi A, Thayer S, Fernandez-Del Castillo C, Harisinghani MG. Enhanced primary tumor delineation in pancreatic adenocarcinoma using ultrasmall super paramagnetic iron oxide nanoparticle-ferumoxytol: an initial experience with histopathologic correlation. Int J Nanomedicine 2014;9:1891–6.
47. Briley-Saebo KC, Johansson LO, Hustvedt SO, Haldorsen AG, Bjørnerud A, Fayad ZA, et al. Clearance of iron oxide particles in rat liver: effect of hydrated particle size and coating material on liver metabolism. Invest Radiol 2006;41:560–71.
48. Kuhlpeter R, Dahnke H, Matuszewski L, Persigehl T, von Wallbrunn A, Allkemper T, et al. R2 and R2* mapping for sensing cell-bound superparamagnetic nanoparticles: in vitro and murine in vivo testing. Radiology 2007;245:449–57.
49. Girard OM, Ramirez R, McCarty S, Mattrey RF. Toward absolute quantification of iron oxide nanoparticles as well as cell internalized fraction using multiparametric MRI. Contrast Media Mol Imaging 2012;7:411–7.
50. Chang TC, Shiah HS, Yang CH, Yeh KH, Cheng AL, Shen BN, et al. Phase I study of nanoliposomal irinotecan (PEP02) in advanced solid tumor patients. Cancer Chemother Pharmacol 2015;75:579–86.